Materials and Design 196 (2020) 109118

Contents lists available at ScienceDirect

Materials and Design

journal homepage: www.elsevier.com/locate/matdes

A multiscale study of hot-extruded CoNiGa ferromagnetic shape-memory alloys

Stavros Samothrakitis [a,b,*], Camilla Buhl Larsen [a,b], Robin Woracek [a,c], Luděk Heller [a,b], Jaromír Kopeček [b], Gregory Gerstein [d], Hans Jürgen Maier [d], Michal Rameš [b], Michael Tovar [e], Petr Šittner [a,b], Søren Schmidt [f], Markus Strobl [a,g,h,*]

[a] Nuclear Physics Institute, Academy of Sciences of the Czech Republic, 25068, Řež near Prague, Czech Republic
[b] FZU Institute of Physics, Czech Academy of Sciences, Na Slovance 1992/2, 1822 Prague, Czech Republic
[c] European Spallation Source ERIC, P.O.Box 176, Lund 22100, Sweden
[d] Institut für Werkstoffkunde (Materials Science), Leibniz University Hannover, An der Universität 2, D-30823 Garbsen, Germany
[e] Helmholtz-Zentrum Berlin, Department Structure and Dynamics of Energy Materials, Hahn-Meitner-Platz 1, 14109 Berlin, Germany
[f] Technical University of Denmark, Department of Physics, Fysikvej, 2800 Kgs. Lyngby, Denmark
[g] Applied Materials Group, Laboratory for Neutron Scattering & Imaging, Paul Scherrer Institut, CH-5232 Villigen, Switzerland
[h] Niels Bohr Institute, University of Copenhagen, 2100 Copenhagen, Denmark

HIGHLIGHTS

- Two CoNiGa FSMA samples, prepared by a novel hot extrusion method, were investigated by multiple characterisation techniques.
- The post-extrusion heat treatment resulted in homogeneous oligocrystalline microstructure and precipitation of γ-CoNiGa.
- γ precipitation decreased the martensitic transformation temperatures by altering the chemical composition of the B2 matrix.
- The two samples exhibited significant differences in microstructural, magnetic, and mechanical properties.
- The heat-treated γ-precipitated sample exhibited improved ductility, higher transformation stress, and higher strength.

GRAPHICAL ABSTRACT

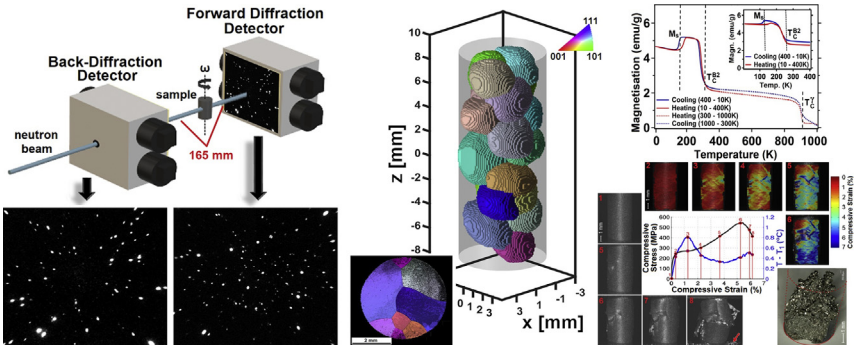

ARTICLE INFO

Article history:
Received 13 June 2020
Received in revised form 25 August 2020
Accepted 31 August 2020
Available online 03 September 2020

Keywords:
Co-Ni-Ga
Ferromagnetic shape-memory alloy

ABSTRACT

Ferromagnetic shape-memory CoNiGa alloys have attracted much scientific interest due to their potential alternative use as high-temperature shape-memory alloys, bearing a high prospect for actuation and damping applications at elevated temperatures. Yet, polycrystalline CoNiGa, due to strong orientation dependence of transformation strains, suffers from intergranular fracture. Here, two multi-grain CoNiGa samples were prepared by a novel hot extrusion process that can promote favourable grain-boundary orientation distribution and improve the material's mechanical behaviour. The samples were investigated by multiple methods and their microstructural, magnetic, and mechanical properties are reported. It is found that a post-extrusion solutionising heat treatment leads to the formation of a two-phase oligocrystalline homogeneous microstructure consisting of an

* Corresponding authors.
E-mail addresses: samothrakitis@ujf.cas.cz (S. Samothrakitis), markus.strobl@psi.ch (M. Strobl).

https://doi.org/10.1016/j.matdes.2020.109118

Martensitic transformation
Hot-extrusion
Laue three-dimensional neutron diffraction tomography

austenitic parent B2 phase and γ-CoNiGa precipitates. Reconstruction of the full 3D grain morphology revealed large, nearly spherical grains with no low-angle grain boundaries throughout the entire sample volume. The presence of γ precipitation affects the transformation behaviour of the samples, by lowering the martensitic transformation temperature, while, in conjunction with the oligocrystalline microstructure, it improves the ductility. Controlling the composition of the B2 matrix, as well as the phase fraction of the γ phase, is thus crucial for the optimal behaviour of the alloys.

1. Introduction

Ferromagnetic shape-memory alloys (FSMA) are attractive materials for use in sensing and/or actuation applications because they feature large magnetic field-induced strains (MFIS) as well as shape-memory effect or pseudoelasticity, similar to conventional shape-memory alloys (SMA) [1–6]. The most extensively studied FSMA is the Heusler-type Ni_2MnGa ternary alloy [7–9]. Ni_2MnGa exhibits giant MFIS (up to 10%) and has good thermal stability [7,9]. However, its severe brittleness in the polycrystalline state limits its range of applications to single crystals and thin films. An attractive alternative to Ni_2MnGa is the ferromagnetic CoNiGa alloy that was originally developed as promising high-temperature SMA (HTSMA) [10]. It transforms from the high-temperature cubic B2 (CoNiGa-β) phase into a low-temperature tetragonal $L1_0$ phase [11–14]. CoNiGa alloys are not as brittle as Ni_2MnGa and the overall ductility of the B2 matrix can be further improved by precipitation of the γ phase (disordered fcc-type A1) [10,11,13,14]. Single crystalline CoNiGa has been found to exhibit excellent shape-memory behaviour, reversible pseudoelastic strains of up to 8.6%, working temperatures of up to 500 °C and overall good functional stability [15–19]. Adding the reasonable cost of its alloying elements makes CoNiGa highly attractive for prospective applications.

Based on composition and heat treatments, CoNiGa alloys can feature elevated Curie temperatures (T_C) and martensitic start temperatures (M_s), making them indeed suitable HTSMA candidate materials [11,13,20,21]. Precipitation of the γ phase does improve the room- and high-temperature ductility of the alloys substantially, and, due to being Co-rich, it shifts the Curie temperature of the alloys to considerably high values. On the other hand, this negatively affects the *Ms* [22] and the overall shape-memory behaviour by altering the matrix composition and the phase fraction of transformable phases [20]; γ-CoNiGa does not undergo martensitic transformation and does not contribute to the shape-memory effect. Consequently, depending on its phase fraction, γ phase precipitation can suppress the martensitic transformation of CoNiGa alloys or degrade their functional properties.

In spite of their superior ductility, the functional properties of CoNiGa alloys are still best utilised with single crystals. In polycrystals, the small plastic deformability of the B2 matrix, in conjunction with the requirement for strain compatibility at grain boundaries and triple points, causes them to suffer from premature grain boundary failure upon thermo-mechanical loading. To overcome this problem, many efforts into tailoring the alloys' microstructure have been made, including the formation of highly textured grain morphologies and oligocrystalline bamboo-like structures, which can lead to significantly improved material performance [23]. In recent studies, a high temperature extrusion process was introduced as a means of promoting the formation of an oligocrystalline bamboo-like microstructure in CoNiGa [24,25]. The extrusion process is conducted at elevated temperatures and followed by a heat treatment, leading to the formation of an oligocrystalline microstructure as well as precipitation of the γ phase. A careful choice of temperatures and area reduction during extrusion, as well as suitable temperatures for the post-extrusion heat treatment, are needed to promote the formation of a near-bamboo-like microstructure giving rise to an adequate pseudoelastic response.

In the present study, the microstructure, as well as mechanical and magnetic properties of two hot-extruded CoNiGa samples were investigated. One sample was characterised in the as-extruded condition and the other after post-extrusion heat treatment. This allows for an insightful discussion of the effect of the different steps of the extrusion process on the mechanical, functional, and magnetic properties of the alloys. For the microstructural characterisation of the samples Laue three-dimensional neutron diffraction tomography (Laue 3DNDT) [26,27] and scanning electron microscopy (SEM) in conjunction with electron backscatter diffraction (EBSD) were employed. Compositional analysis was done using energy dispersive spectroscopy (EDS) in the SEM. For retrieving the magnetostructural transition temperatures and saturation magnetisations, as well as to investigate the magnetic behaviour of the samples, magnetisation measurements were performed. Compression tests in conjunction with digital image correlation (DIC) and thermography were carried out to test and compare the ductility of the two samples and to monitor the deformation-induced martensitic phase transformation and plastic deformation.

2. Materials and methods

The CoNiGa alloy, with nominal composition 49Co-21Ni-30Ga (in at.%), was obtained in polycrystalline as-cast form from Sophisticated Alloys, USA. From the as-cast material, a cylinder with 80 mm length and an initial diameter of 8 mm was cut for hot extrusion. The cylinder was enclosed in a C45 steel can, initially heated up to 1473 K in a conventional furnace and then transferred to the heated extrusion device (2.5 MN Müller Engineering extrusion press). The hot encapsulated billet was then coated with glass fragments to guarantee sufficient lubrication during processing. With this approach the heat loss during transfer and coating was accounted for and the actual extrusion temperature of the CoNiGa alloy could be kept at 1173 K. The extrusion speed was set to 5 mm/s. After extrusion the CoNiGa cylinder was air-cooled. Upon single step extrusion the diameter of the cylinder was reduced by a factor of 2 to a final diameter of 4 mm. Following cooling, two cylindrical samples (15 mm × Ø 4 mm each) were cut. In order to induce the ductile γ phase in the microstructure, one of the samples was solution annealed at 1433 K for 24 h with a heating rate of 3 K/s. Subsequently, the sample was furnace cooled down to 1133 K and held there for 4 h. For the post-extrusion heat treatment, the sample was encapsulated in a quartz tube in argon atmosphere. Henceforth, the as-extruded sample and the post-extrusion heat-treated sample will be referred to as sample A and sample B, respectively.

For microstructural and magnetic characterisation, 1 mm thick disc-shaped slices (1 mm × Ø 4 mm) were cut from each sample. The disc-shaped samples were then investigated in the SEM in combination with EBSD. The exact composition of the samples, in the as-extruded and extruded heat-treated conditions, was measured by EDS. The metallographic samples were hot-mounted into conductive Bakelite and the polishing was finalised by colloidal silica. For the measurements a Tescan FERA3 SEM, equipped with EDAX analysers (Octane Super 60 mm^2 for EDS and DigiView IV for EBSD), was used. Magnetisation of the samples was measured as a function of temperature and magnetic field with a commercial vibrating sample magnetometer (VSM) on a PPMS 9 system from Quantum Design. For the thermomagnetic measurements, the temperature ranged between 10 and 1000 K, with a

heating/cooling rate of 4 K/min, under an applied magnetic field of 10 mT. The magnetic-field-dependent magnetisation measurements were performed at four different temperatures – 10, 100, 200, and 300 K – within a magnetic field range of 0 to 9 T.

The bulk cylindrical samples (14 mm × Ø 4 mm each) were measured by means of Laue 3DNDT. Laue 3DNDT is a recently developed method, able to return information regarding a sample's grain positions, orientation distribution and texture, as well as morphology, from a large sample volume, for grains larger than a few 100 μm [26,27]. The Laue neutron diffraction measurements were performed at the E11 beam-port of the BERII reactor of the Helmholtz-Zentrum Berlin. For data acquisition the FALCON [28] double-detector system was employed. The thermal neutron spectrum was used with the full wavelength range available ($0.9 \leq \lambda \leq 3.2$ Å). Each of the samples was fully illuminated by the neutron beam with 0.3° divergence, allowing for diffraction from all grains constituting the samples, simultaneously. Both samples were measured at ambient temperature and with no load imposed while rotated within an angular range of 320° and angular step $\Delta\omega = 1°$, with a total scanning time of 2.7 h (30 s per exposure). Fig. 1 depicts a schematic of the FALCON far-field diffraction setup, with the sample positioned in the centre of the setup, on a rotational stage that allows for tomographic measurements to be recorded. In Fig. 1a and b Laue images for samples A and B, respectively, are displayed as recorded on the forward diffraction detector at $\omega = 0°$, after background subtraction. In both sets of Laue diffraction measurements the detector-to-sample distance was 165(2) mm, for both the forward and back-scattering detector. The Laue 3DNDT data analysis was carried out in a two-step process; the grain indexing was performed following the data processing described in Ref. [26] and the morphological grain reconstruction was carried out according to Ref. [27].

In order to characterise the failure mode and the ductility of the specimens, monotonous compression tests until fracture were performed. The tests were carried out using a servohydraulic Instron 8872 machine operated in the position control mode using a strain rate of 0.05%/s. Strains on the samples' surface were tracked by digital image correlation (DIC) using a synchronised 12 Mpx Ximea MX124MG-SY-X2. Prior to testing, the samples' surface was black/white speckle-patterned with an Iwata Custom Micron CM-C Plus airbrush. The recorded images were processed using the Mercury software that delivered 2D Lagrange strain fields for individual images using the sample surface prior to loading as a reference. The temperature of samples was simultaneously monitored using a Infratec ImageIR 8300 (640 × 512 px) cooled infrared camera. The evolution of the temperature was evaluated using the temperature averaged over the whole monitored area of the sample that coincided with area tracked by DIC.

The composition (nominal and measured) of both samples, along with their structural transformation temperatures, magnetic ordering temperatures, valence electron concentration, e/a, and magnetic valence number, Z_m, are given in Table 1.

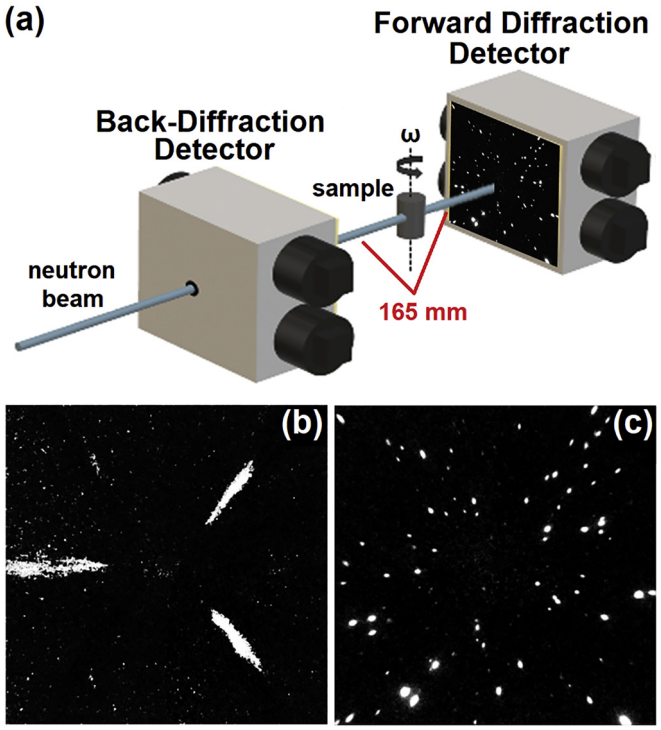

Fig. 1. (a) Schematic representation of the Laue 3DNDT setup; (b) and (c) neutron Laue diffraction images of sample A and sample B, respectively, recorded on the forward scattering detector at $\omega = 0°$, at ambient temperature with no superimposed external load; background subtraction has been applied.

3. Results and discussion

3.1. Alloy microstructure from EBSD

Fig. 2a, b show the granular microstructures of samples A and B along with the grain orientation distribution with respect to the bar axis, colour-coded according to the inverse pole figure (IPF). The EBSD IPF map of sample A (Fig. 2a) shows that the microstructure is heterogeneous, with grain size and shape greatly varying over the cross section. The sample also contains coarse elongated "parent" grains, >1–2 mm in length, containing fine subgrains of mutually similar orientations with grain sizes extending down to the sub-micron scale. Other parts of the sample exhibit random grain orientations. The sample's overall inhomogeneous microstructure is in good agreement with results reported by Karsten et al. [24] and Niendorf et al. [25] who attributed this to the non-homogeneously distributed dynamic recrystallisation induced by the extrusion process. Along the direction of the sample axis, matching the extrusion direction, the grain elongation is expected to be higher. No martensitic twins are visible within the field-of-view, which is in agreement with the results of the phase analysis (Fig. 2c), returning solely the B2 phase, with no secondary A1 γ or $L1_0$ martensitic phases present.

The EBSD IPF map of sample B (Fig. 2b) clearly shows that the post-extrusion heat treatment resulted in significant grain growth and gave

Table 1
Nominal and measured compositions, structural transformation temperatures (M_s, M_f, A_s, A_f), magnetic ordering temperatures (T_C^{B2}, T_C^{γ}), valence electron concentration number (e/a), and magnetic valence number (Z_m) of samples A and B. All the magnetic and structural transition temperatures were calculated with the two-tangent intersection method from the magnetisation curves of Fig. 4.

	Sample A	Sample B
Condition	As-extruded	Extruded heat-treated
Nominal composition (at.%)	49Co-21Ni-30Ga	49Co-21Ni-30Ga
Measured composition of B2 (at.%)	52.62Co-22.08Ni-25.29Ga	48.92Co-23.85Ni-27.23Ga
Measured composition of γ (at.%)	–	58.96Co-19.61Ni-21.42Ga
M_s (K)	276	163
M_f (K)	245	144
A_s (K)	277	163
A_f (K)	303	194
T_C^{B2} (K)	412	310
T_C^{γ} (K)	–*	912
e/a of B2 matrix	7.7025	7.6047
Z_m of B2 matrix	−0.2325	−0.3277

* After γ precipitation occurs, T_C^{γ} is found to be 975 K while the magnetic ordering temperature of the B2 matrix, T_C^{B2}, drops to 211 K.

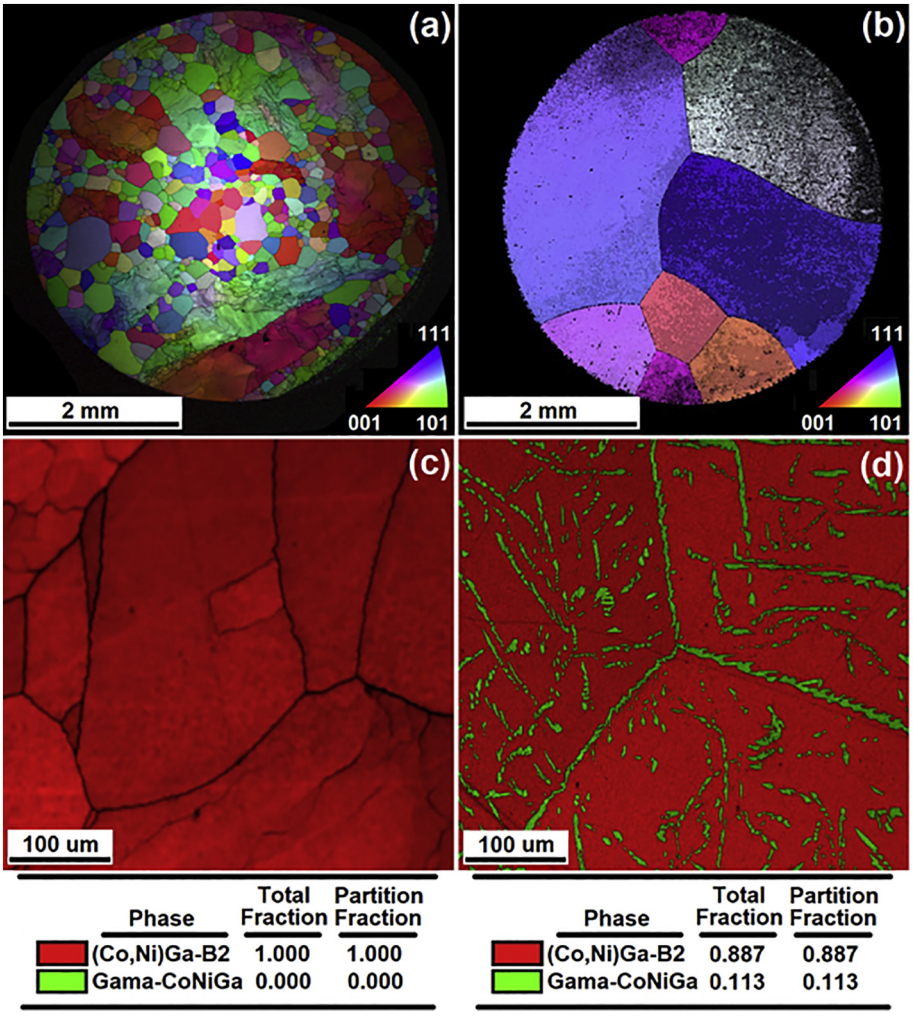

Fig. 2. EBSD inverse pole figure (IPF) maps showing the grain structure of (a) sample A and (b) sample B. The grains are colour-coded according to the IPF for an out-of-plane view (top $+z$ direction); (c) and (d) phase analysis for samples A and B, respectively. The areas in (c) and (d) do not strictly correspond to specific areas in (a) and (b) as the samples had to be removed, repolished, and repositioned in the SEM chamber.

rise to an oligocrystalline microstructure along with a notable reduced number density of grain boundaries and triple points. The grain orientation distribution shows no strong preferred grain orientation with only two grains showing near-<100> orientation along the out-of-plane projection. The phase analysis (Fig. 2d) returned volume fractions of 88.7% for the B2 matrix phase and 11.3% for the γ-CoNiGa precipitates within grain interior regions as well as those decorating grain boundaries. No martensitic twins were found, indicating that the $L1_0$ martensitic phase, for both samples, only appears below room temperature. In addition, it can be noted that none of the samples exhibits intergranular cracking. This indicates that no cracks were introduced during the hot extrusion process and subsequent cooling to room temperature.

The microstructure in the post-extrusion heat-treated condition is in good agreement with similar hot-extruded CoNiGa samples from Ref. [24 and 25], having grain sizes also in the mm scale and decorated with γ-CoNiGa precipitates. Karsten et al. [24] investigated the effect of different initial (prior to extrusion) sample diameters upon the grain formation. Their findings indicate that samples with initial diameters ranging between 8 and 15 mm had, to some extent, differences in their grain morphology in the as-extruded condition. Simulations of the extrusion process showed that the main influencing factor on the dynamic recrystallisation was the forming temperature during extrusion which was more homogeneously distributed for smaller-diameter samples. This in turn impacts the degree of grain growth and microstrucure evolution during the final stage of heat treatment. According to them, recrystallisation and grain growth occur heterogeneously throughout the material, and can be described in terms of nucleation and growth stages; discontinuous subgrain growth, primary recrystallisation, and abnormal grain growth [29]. The latter is found to be greatly influenced by grain size distribution. Fine microstructures, also containing subgrain formations (as in sample A), will result in more pronounced abnormal grain growth, which finally leads to an oligocrystalline homogeneous microstructure [30,31], as seen in sample B.

The 2D microstructure information obtained from EBSD (Fig. 2), while providing a good estimation of the samples' grain morphology, is insufficient to fully characterise the specimens. 3D information is necessary to relate it to mechanical properties. 3D EBSD analysis could be employed to retrieve such information but, due to being destructive, the mechanical properties of the samples cannot be determined. Alternatively, it is possible to perform a non-destructive microstructure reconstruction using a 3D Laue method. Revisiting Fig. 1b and c it is seen that the Laue patterns, and consequently the microstructures, of the two samples are profoundly different. The reflections originating from sample A (Fig. 1b), with small and big diffraction spots in sight, including sizeable, elongated reflections, demonstrate its inhomogeneous microstructure. The elongated features are found to be clusters of fine reflections. This confirms the presence of a highly textured sub-grain microstructure, as seen in the EBSD map (Fig. 2a), and hints to elongated grains also along the sample's long axis. In contrast, the Lauegram of

sample B (Fig. 1c), showing less number of clearly distinguishable diffraction spots, suggests a rather homogeneous large grain microstructure, in line with the EBSD map of Fig. 2b.

3.2. Alloy microstructure from Laue 3DNDT

Fig. 3a shows the reconstructed 3D model of the microstructure of sample B in isoprojection. Ortho-slices of the microstructure along the *x-y* and *x-z* planes are given in Fig. 3b. The final 3D reconstruction can also be seen in the Supplementary Video 1. In total, 20 grains were indexed and reconstructed within the entire sample volume. The average grain size is 3.3(1) mm with a standard deviation of 0.46 mm, highlighting a rather uniform grain size. The reconstructed grains were indexed with a B2 cubic crystal structure with a lattice parameter of $a = 2.8657(2)$ Å. No $L1_0$ or A1 phases were detected, suggesting that at room temperature, within the Laue 3DNDT resolution limit, the sample is dominated by the B2 phase. From the reconstructed 3D grain microstructure model, it is clearly seen that the morphology of the grains is relatively isotropic, i.e. not bamboo-like elongated along the *z*-axis. Minor grain details, particularly from the outer regions, might be missing due to spatial resolution limitations in these far-field measurements with a relatively divergent neutron beam. The orientation distribution of the grains, highlighted by the IPF colour-map and the IPF given in Fig. 3c, shows no signs of a strong preferred crystallographic orientation. Additionally, none of the grains exhibits a near-<100> orientation along the sample's long axis direction. Calculating the misorientation angles between the indexed grains we find that no adjacent grains (apart from one pair) have a misorientation angle less than 15°, thus practically no low-angle grain boundaries exist in the microstructure. It appears that the post-extrusion annealing and ageing of sample B had resulted in a non-textured oligocrystalline and reasonably homogeneous microstructure with high-angle grain boundaries only.

3.3. Structural and magnetic phase transitions

Results of the magnetisation measurements at 10 mT as a function of temperature, for both samples, are shown in Fig. 4. The measurements were performed in two consecutive steps; i) cooling from 400 K to 10 K and heating back to 400 K, ii) heating from 400 K to 1000 K and cooling back to 400 K. The magnetisation curve of sample A (Fig. 4a) shows martensitic transformation occurring below room temperature

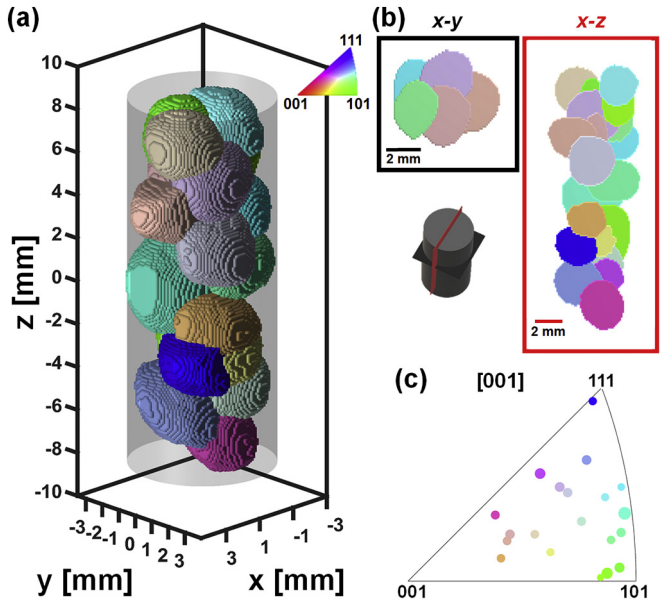

Fig. 3. Laue 3DNDT grain morphology reconstruction map of sample B in (a) isoprojection and (b) along the *x-y* and *x-z* planes, as given by the schematic in the figure. The grains are colour-coded according to their orientation given by the IPF for a top view of the sample; (c) IPF showing the orientations of the 20 grains along the [001] direction. The markers are scaled according to the corresponding grain size.

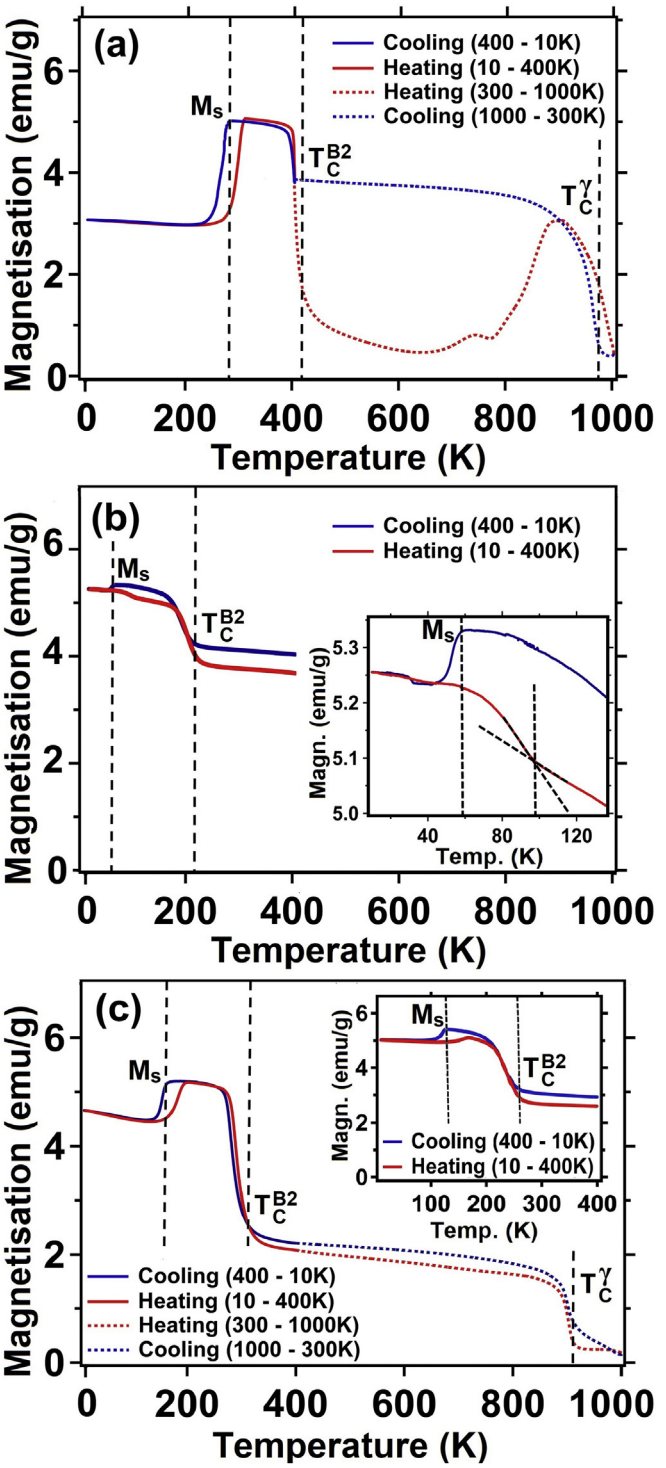

Fig. 4. Magnetisation curves obtained as a function of temperature for (a),(b) sample A and (c) sample B. Panel (b) refers to the second measurement of sample A to highlight microstructural changes induced during the first measurement due to in-situ heating. The inset in (b) shows an extra inflection point seen at about 97 K, during heating. The inset in (c) depicts a second cooling-heating cycle performed for sample B between 10 and 400 K showing additional changes to the magnetisation due to in-situ heating. The magnetostructural transition temperatures are calculated from the curves with the two-tangent intersection method and are given in Table 1; a constant magnetic field of 10 mT was applied during the measurements.

($M_s = 274$ K and $M_f = 245$ K) and reverse transformation upon heating at about 300 K ($A_s = 277$ K and $A_f = 303$ K). The differences in magnetisation levels between martensite and austenite are due to their different magnetocrystalline anisotropies, giving rise to the distinct step changes in magnetisation, highlighting the reversible martensitic transformation, which can be easily tracked down with these low-field thermomagnetic measurements. While at low fields austenite, due to its lower magnetocrystalline anisotropy, is magnetically softer, the opposite behaviour is observed at high applied magnetic fields [32–34], with martensite exhibiting higher than austenite saturation magnetisation (cf. Fig. 5) demonstrating a change of magnetocrystalline anisotropy [34].

The sample is ferromagnetically ordered below 412 K (T_C of B2 matrix), at which the paramagnetic-to-ferromagnetic transition occurs upon cooling. Further increasing the temperature, above T_C^{B2}, induces a new phase at about 700 K. This is attributed to precipitation of Co-rich γ-CoNiGa, which is known to have similar magnetisation behaviour and Curie temperatures as the one observed here ($T_C^{\gamma} = 975$ K) [35–37]. The small drop in magnetisation just below 800 K before further increasing, as similarly observed by Wang et al. [35], might be ascribed to an extra structural transition of the γ particles, possibly from the disordered A1 (Co,NiGa) into the ordered $L1_2$ ($(Co,Ni)_3Ga$) phase with two sublattices, that would be related to the thermal (in)stability of the γ precipitates during VSM heating [35]. During cooling from 1000 K the γ phase persists and the sample remains ferromagnetically ordered for the entire temperature range below 1000 K. This indicates that the irreversible precipitation of γ phase, taking place at high temperature, can be fully tracked down in the in-situ VSM experiment.

A second low-field magnetisation measurement between 10 K and 400 K (Fig. 4b) was performed to verify the assumption of irreversible changes at high temperatures. The sample indeed exhibits a different magnetic behaviour from the first cycle. The magnetisation of the sample remains non-zero (> 4 emu/g) within the 10–400 K temperature interval. The B2-γ coexistence is thus apparent while the martensitic transformation is not as profound as before, making clear that the γ phase had stabilised the austenitic phase and suppressed the martensitic transformation. The magnetisation below and over $M_s = 58$ K is almost at the same level, indicating that even at really low temperatures the sample is still dominated by the B2 cubic phase and any martensitic transformation does not fully progress. Additional cooling-heating cycles showed that no more changes occurred indicating that the sample had become stable. An inflection point seen at 97 K upon heating (cf. inset of Fig. 4b) is attributed to spin reorientation, also observed in Ni-Fe-Ga single crystals [38].

The magnetisation curve of sample B, cf. Fig. 4c, clearly shows that the sample contains B2 phase matrix and γ phase precipitates from the very beginning of the VSM experiment. The martensitic transformation upon cooling starts at $M_s = 163$ K, which is significantly lower than that of sample A before recrystallisation. The magnetic ordering temperature of the B2 matrix is 310 K while that of the γ phase is 912 K. The low-field magnetisation in the martensitic region is lower than in the austenitic one above A_f, again highlighting the different magnetocrystalline anisotropies of the two phases. Above T_C^{B2} the magnetisation is non-zero, which is clearly connected to the precipitated γ-CoNiGa, with the sample exhibiting a similar behaviour to that of sample A after recrystallisation and precipitation. A small hysteresis seen above T_C^{γ} hints to possible additional precipitation of γ phase due to VSM in-situ heating. As such, similarly to sample A, a second cooling-heating cycle between 10 K and 400 K was performed for sample B (cf. inset of Fig. 4c). The measurement shows clear magnetisation changes, which are attributed to further precipitation of γ-CoNiGa, shifting the M_s and the T_C^{B2} to even lower values, at about 126 K and 260 K, respectively. This too demonstrates the significant effect that γ phase precipitation has on the martensitic transformation.

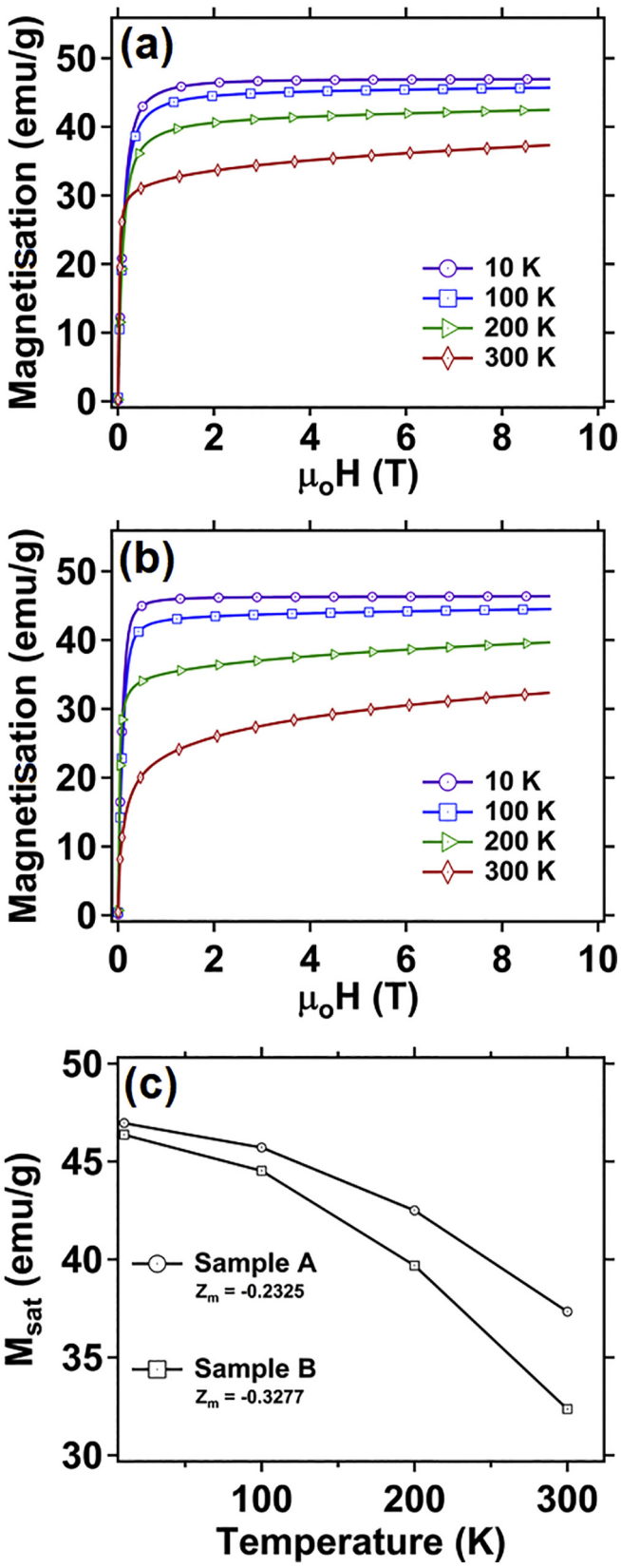

Fig. 5. Magnetisation curves as a function of magnetic field for (a) sample A and (b) sample B; (c) saturation magnetisation of both samples as calculated from the magnetisation curves given in panels (a) and (b).

To evaluate the M_s with respect to the composition of the samples, the valence electron concentration number, e/a, was calculated using the following expression: $\sum(f_X \times e_v^X)/100$, where f_X is the atomic fraction of element X and e_v^X its number of valence electrons. e/a is thus directly connected to the composition of the samples. It has been a commonly used parameter in SMA research for predicting and evaluating martensitic transformation temperatures, with both theoretical and experimental findings suggesting a strong correlation between e/a and martensitic start temperature. For example, for NiMnGa alloys it is found that e/a and M_s have an almost perfect linear relationship [39]. The exact correlation of e/a and M_s for CoNiGa alloys, though, is unclear, with the content of Ga in the alloys seeming to be important; in some cases, the linearity of M_s and e/a holds only for the same Ga level, and for a constant e/a, higher Ga content results in higher M_s [10,13,40]. Examining the e/a ratio values of samples A and B, given in Table 1, it is seen that the value of sample A is higher, which could potentially explain its higher M_s. Considering a linear relationship between M_s and e/a, though, in accordance to Ref. [10, 13, 40], and, the overall martensitic transformation temperatures, for both samples, are expected to be significantly higher, demonstrating that the linear relationship is not strictly fulfilled. According to Chernenko et al. [41], an inflection seems to exist at an e/a value of about 7.7 for NiMnGa alloys, which could also be the case for CoNiGa. Yet, looking at the results of Craciunescu et al. [42], a good linear relationship between the two parameters is observed, even for an e/a value up to 7.8, although only the nominal composition of the alloys was considered and whether the samples had a single or double phase was not mentioned. All the above make clear that simple compositional considerations, in terms of the valence electron concentration, do not suffice for predicting and tuning the M_s.

Another key aspect that seems to affect the M_s temperature is the magnetic character of the samples. A specimen with a strongly magnetic B2 matrix, having high Co content, high T_C and high magnetic moment, is assumed to have a more stable austenitic parent phase and thus lower martensitic transformation temperature [40]. To estimate the magnetic behaviour of the samples the magnetic valence number, Z_m, of the parent phase can be used. In principle, the magnetic valence gives the contribution of each element to the total magnetisation of a sample when only d-band electrons are considered [43]. It is a (positive or negative) integer number for each column of the periodic table, given by $Z_m = 2N^{\uparrow} - Z$, where $N^{\uparrow}$ is the spin-up d-band valence electrons and Z the chemical valence. For Co, Ni, and Ga the magnetic valence is 1, 0, and −3, respectively. The total magnetic valence number of a sample is then given by the sum of the magnetic valence of each element scaled by its atomic fraction within the sample. Hence, higher Co and/or lower Ga contents result in a higher (i.e. more positive) magnetic valence number, which is found to lead to higher T_C, higher magnetic moment, and higher saturation magnetisation [13,43]. Sample A, with more positive Z_m, should thus exhibit enhanced magnetic properties when compared to sample B, which is evidently apparent by the higher T_C of its B2 matrix. Furthermore, looking at the field-dependent magnetisation measurements in Fig. 5, one sees that the saturation magnetisation of sample A is consistently higher than that of sample B (cf. Fig. 5c), for the entire temperature range of 10–300 K, with the largest difference being at room temperature, where the B2 austenitic phase prevails. The overall higher saturation magnetisation of sample A could be partially attributed to the higher Co content of its B2 matrix, as reflected by its Z_m. Sample B though, contains fractions of Co-rich γ-phase, which is expected to increase its saturation magnetisation. As shown by Wang et al. [36], double-phase samples, having similar compositions, exhibit higher saturation magnetisation when the γ-phase fraction is higher, but a linear correlation between saturation magnetisation and Z_m cannot be firmly assumed. On the other hand, it is seen that a large increase of γ-phase fraction, more than 20%, only increases the saturation magnetisation by less than 2 emu/g. A higher ordering degree in austenite (e.g. $L2_1$ instead of B2) for sample A, could also potentially explain its higher saturation magnetisation [44], however no evidence of such crystal structure was detected by our applied methods.

In spite of sample A having a more positive Z_m than sample B, and in contrast to what is expected, its M_s is also notably higher. This shows that, as in the case of e/a, Z_m alone is not sufficient to predict the M_s, and a synergy between e/a and Z_m might exist. Based on their experimental results, Dogan et al. [40] attempted to draw empirical expressions using linear regression to predict the martensitic start temperatures. The derived equations were either a function of e/a and Z_m, or a function of the Co and Ga contents. Employing the numbers given in Table 1, in conjunction with the aforementioned expressions, we find that the martensitic start temperatures, for both sample A and sample B, should exceed 400 K, which contradicts the present results, although Dogan et al. [40] used only single-phase CoNiGa specimens.

The above make clear that the main key parameter is the γ phase precipitation and its phase fraction. As evident by the magnetisation measurements, given in Fig. 4, and more profoundly from the second magnetisation measurements of samples A and B (Fig. 4b and inset of Fig. 4c), γ precipitates immediately shift the M_s to lower values and hinder the martensitic transformation. This can be, in one part, attributed to compositional changes of the B2 matrix, that should also be reflected upon e/a (and/or Z_m), as was clearly evidenced in the study of Liu et al. [20]; precipitation of γ after different heat treatments resulted in a gradual increase of the Ga content in the B2 matrix which in turn led to a decrease of both e/a and M_s. Since the γ phase is non-transformable though, its phase fraction as well as the grain region, where the precipitates are situated, are also essential to the functional behaviour of the samples. Large γ fractions drastically reduce the phase fraction of the martensitically transformable B2 phase, having a direct effect upon the transformation behaviour and magnetic properties of the samples.

3.4. Compression stress-strain behaviour

Fig. 6a, b present compression behaviour until fracture of samples A and B, respectively. Stress-strain curves in the centre are supplemented with the record of in-situ sample temperature evaluated by infrared camera. The surrounding pictures show spatially resolved axial strain maps evaluated by DIC and optical images of the samples in selected loading stages, as well as fracture surfaces. It is seen that sample B exhibits significantly higher yield stress, more than two times higher strength, and two times larger strain at failure than sample A. The stress-strain curves feature stress plateaus appearing between loading stages 2 and 3. This is due to the fact that the plastic deformation starts by the stress-induced martensitic transformation. This can be deduced from the: i) larger yield stress of sample B with lower M_s temperature, ii) local temperature maxima at the onset of plastic deformation due to the latent heat and iii) deformation bands with highly localised strain, typical for stress-induced transformation, observed by DIC. The temperature changes must be interpreted with caution as they integrally reflect the heat effects of all involved deformation processes; in our case, besides martensitic transformation, also the heat dissipated by plastic deformation via dislocation slip. Sample B shows four times lower local temperature peak compared to sample A and temperature increase with strain in later stages of deformation is also lower. This suggests that the stress-induced martensitic transformation is more active in the small-grain-size sample A than in sample B. The most likely reason for this is the larger transformation stress needed to activate the stress-induced transformation in sample B.

The strain maps reveal localised deformation via shear bands that span over multiple grains of sample A and individual grains in the case of sample B. While the deformation remains localised until the rupture in sample B, it becomes rather homogeneous in the case of sample

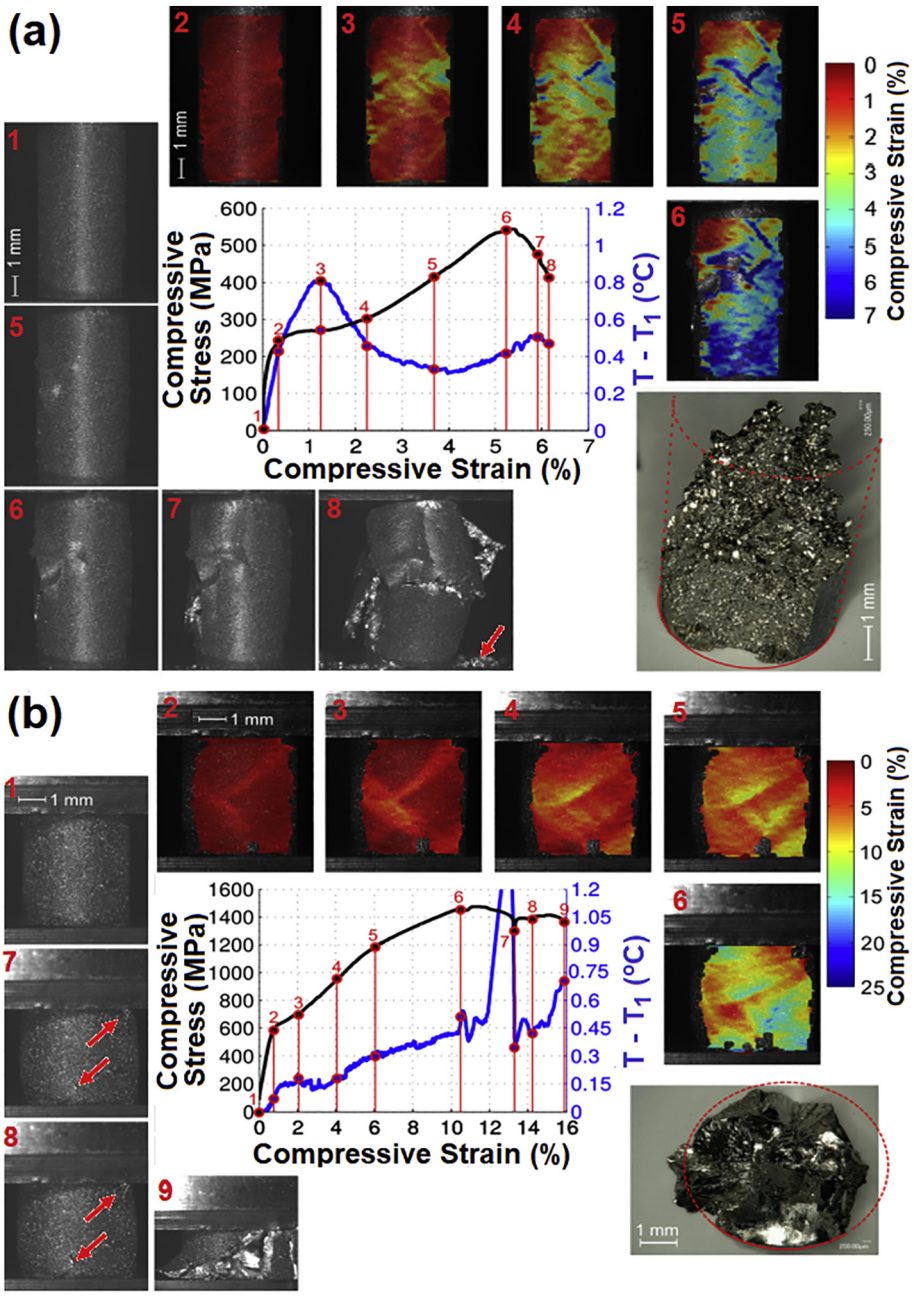

Fig. 6. Compression test at room temperature until fracture of (a) the as-extruded sample A and (b) the post-extrusion heat-treated sample B. Samples' temperature (blue curves) is monitored and surface strain is evaluated by DIC during the test. The 2D strain maps show axial strain component in selected stages of the test. Optical images show the sample surfaces prior to loading (stage 1) and prior to rupture (stages 6–9) - see also complete Supplementary Videos 2 and 3 informing strain evolution during the test. Fracture surfaces are shown in the lower right corners. (For interpretation of the references to colour in this figure legend, the reader is referred to the web version of this article.)

A. Cracks become visible on the surface of both samples at stage 6, when maximum stress is reached. The cracking is accompanied by higher temperature increase in the case of sample B giving rise to the sharp temperature peak. The failure of sample A is via brittle fracture with the sample literally falling apart (cf. red arrow pointing to crystallites in photograph 8 of Fig. 6a). Sample B accommodates much more plastic deformation prior to failure, as shown in photographs 7–9 in Fig. 6b. The fracture surfaces in Fig. 6a and b (bottom right) reveal fracture facets, the size of which reflects the grain size of both samples.

The lesser tendency towards strain localisation and strain hardening capability of sample B is attributed to the lesser activity of stress induced martensitic transformation in the deformation process. The plastic deformation by slip might be further promoted by the presence of γ phase precipitates within sample B (Fig. 2), as speculated in the literature [45,46]. In any case, although sample B is more ductile than sample A, both samples suffer from intergranular cracking and brittle fracture. The extreme elastic and transformation anisotropy of this alloy, combined with the tendency towards strain localisation, suppresses the ductility of this material at room temperature beyond 6% strain. Solution-annealed samples, having microstructure and texture comparable to sample B, exhibit similar behaviour [23]. While the small number of grains, and thus critical grain boundaries and triple points, in the sample cross-section, has a positive impact on the overall ductility and pseudoelastic response of the specimens, the high degree of misorientation of adjacent grains causes stress concentrations near grain boundaries and damage evolution.

4. Conclusions

Two CoNiGa FSMA samples, prepared by a novel method of hot-extrusion, were examined in the as-extruded and the post-extrusion heat-treated conditions, using a multiscale investigation in order to reveal their mechanical, structural, and magnetic properties. It was found that post-extrusion solutionising heat-treatment results in significant grain growth and precipitation of γ phase, giving rise to an oligocrystalline homogeneous microstructure throughout the entire volume of the sample, with reduced number density of grain boundaries and triple points. The 3D microstructure of the sample in the heat-treated condition was evaluated by Laue three-dimensional neutron diffraction tomography, which revealed the dominance of nearly spherical grains with no clear sign of preferred crystallographic orientation.

Structural phase transformation temperatures and magnetic transition temperatures of different phases were evaluated by VSM magnetic measurements in the temperature range 10 K – 1000 K. It was found that γ phase precipitation affects both structural and magnetic transitions. The shift of the martensitic transformation to lower temperatures by the γ precipitates is attributed to a combination of the phase fraction of the γ phase, compositional changes of the parent B2 matrix, and magnetic changes.

Compression tests at room temperature, in combination with digital image correlation and thermography, showed that the post-extrusion heat-treated alloy exhibits improved ductility, higher transformation stress and higher strength compared to the as-extruded alloy although the alloy exhibits brittleness when deformed beyond 6% strain.

Overall, controlling the composition of the samples, as well as the phase fraction and stability of the γ-CoNiGa phase, seeming to be the dominant factor that significantly alters the samples' properties, is of paramount importance to the optimal functionality of CoNiGa alloys.

Data availability

The data that support the findings of this study are available from the corresponding authors upon reasonable request.

Declaration of Competing Interest

The authors state that there are no conflicts of interest associated with this study and the publication of this manuscript.

Acknowledgments

This study was supported by OP RDE, MEYS, under the project "European Spallation Source - participation of the Czech Republic - OP", Reg. No. CZ.02.1.01/0.0/0.0/16_013/0001794; and the MEYS project Solid21 CZ.02.1.01/0.0/0.0/16_019/0000760. The magnetic measurements were carried out at MGML (http://mgml.eu), which is supported by MEYS within the program of Czech Research Infrastructures (project no. LM2018096). Michal Rameš would like to acknowledge support from CSF (grant No. 19-09882S). Hans Jürgen Maier and Gregory Gerstein would like to acknowledge financial support by the Deutsche Forschungsgemeinschaft (DFG, German Research Foundation) within grant 388671975.

Appendix A. Supplementary data

Supplementary data to this article can be found online at https://doi.org/10.1016/j.matdes.2020.109118.

References

[1] J. Enkovaara, A. Ayuela, A.T. Zayak, P. Entel, L. Nordström, M. Dube, J. Jalkanen, J. Impola, R.M. Nieminen, Magnetically driven shape memory alloys, Mater. Sci. Eng. A 378 (2004) 52–60.
[2] E. Faran, D. Shilo, Ferromagnetic Shape Memory Alloys—Challenges, Applications, and Experimental Characterization, Experimental Techniques, 2015.
[3] M. Wuttig, L. Liu, K. Tsuchiya, R.D. James, Occurrence of ferromagnetic shape memory alloys, J. Appl. Phys. 87 (2000) 4707–4711.
[4] O. Heczko, Magnetic shape memory effect and magnetization reversal, J. Magn. Magn. Mater. 290 (2005) 787–794.
[5] A.A. Likhachev, K. Ullakko, Quantitative model of large magnetostrain effect in ferromagnetic shape memory alloys, EPJ Direct 1 (2000) 1–9.
[6] P. Chowdhury, H. Sehitoglu, Deformation physics of shape memory alloys–fundamentals at atomistic frontier, Prog. Mater. Sci. 88 (2017) 49–88.
[7] A. Sozinov, A.A. Likhachev, N. Lanska, K. Ullakko, Giant magnetic-field-induced strain in NiMnGa seven-layered martensitic phase, Appl. Phys. Lett. 80 (2002) 1746–1748.
[8] O. Heczko, A. Sozinov, K. Ullakko, Giant field-induced reversible strain in magnetic shape memory NiMnGa alloy, IEEE Trans. Magn. 36 (2000) 3266–3268.
[9] H. Xu, Y. Ma, C. Jiang, A high-temperature shape-memory alloy $Ni_{54}Mn_{25}Ga_{21}$, Appl. Phys. Lett. 82 (2003) 3206–3208.
[10] E. Dogan, I. Karaman, Y.I. Chumlyakov, Z. Luo, Microstructure and martensitic transformation characteristics of CoNiGa high temperature shape memory alloys, Acta Mater. 59 (2011) 1168–1183.
[11] K. Oikawa, T. Ota, F. Gejima, T. Ohmori, R. Kainuma, K. Ishida, Phase equilibria and phase transformations in new B2-type ferromagnetic shape memory alloys of Co-Ni-Ga and Co-Ni-Al systems, Mater. Trans. 42 (2001) 2472–2475.
[12] V.A. Chernenko, J. Pons, E. Cesari, I.K. Zasimchuk, Transformation behaviour and martensite stabilization in the ferromagnetic Co–Ni–Ga Heusler alloy, Scr. Mater. 50 (2004) 225–229.
[13] K. Oikawa, T. Ota, Y. Imano, T. Omori, R. Kainuma, K. Ishida, Phase equilibria and phase transformation of Co–Ni–Ga ferromagnetic shape memory alloy system, J. Phase Equilib. Diffus. 27 (2006) 75–82.
[14] I.V. Kireeva, J. Pons, C. Picornell, Y.I. Chumlyakov, E. Cesari, I.V. Kretinina, Influence of γ nanometric particles on martensitic transformation and twinning structure of $L1_0$ martensite in Co–Ni–Ga ferromagnetic shape memory single crystals, Intermetallics 35 (2013) 60–66.
[15] J. Dadda, H.J. Maier, I. Karaman, H.E. Karaca, Y.I. Chumlyakov, Pseudoelasticity at elevated temperatures in [001] oriented $Co_{49}Ni_{21}Ga_{30}$ single crystals under compression, Scr. Mater. 55 (2006) 663–666.
[16] J.A. Monroe, I. Karaman, H.E. Karaca, Y.I. Chumlyakov, H.J. Maier, High-temperature superelasticity and competing microstructural mechanisms in $Co_{49}Ni_{21}Ga_{30}$ shape memory alloy single crystals under tension, Scr. Mater. 62 (2010) 368–371.
[17] P. Krooß, T. Niendorf, P.M. Kadletz, C. Somsen, M.J. Gutmann, Y.I. Chumlyakov, W.W. Schmahl, G. Eggeler, H.J. Maier, Functional fatigue and tension–compression asymmetry in [001]-oriented $Co_{49}Ni_{21}Ga_{30}$ high-temperature shape memory alloy single crystals, Shape Memory and Superelasticity 1 (2015) 6–17.
[18] P. Krooß, P.M. Kadletz, C. Somsen, M.J. Gutmann, Y.I. Chumlyakov, W.W. Schmahl, H.J. Maier, T. Niendorf, Cyclic degradation of $Co_{49}Ni_{21}Ga_{30}$ high-temperature shape memory alloy: on the roles of dislocation activity and chemical order, Shape Mem. Superelasticity 2 (2016) 37–49.
[19] T. Niendorf, J. Dadda, J. Lackmann, J.A. Monroe, I. Karaman, E. Panchenko, H.E. Karaca, H.J. Maier, Tension-compression asymmetry in $Co_{49}Ni_{21}Ga_{30}$ high-temperature shape memory alloy single crystals, Materials Science Forum, Vol. 738, Trans Tech Publ 2013, pp. 82–86.
[20] J. Liu, M. Xia, Y. Huang, H. Zheng, J. Li, Effect of annealing on the microstructure and martensitic transformation of magnetic shape memory alloys CoNiGa, J. Alloys Compd. 417 (2006) 96–99.
[21] M. Wuttig, J. Li, C. Craciunescu, A new ferromagnetic shape memory alloy system, Scr. Mater. 44 (2001) 2393–2397.
[22] H. Kalaantari, S. Amini, J. Hong, R. Abbaschian, Investigating the effects of bulk supercooling and rapid solidification on Co–Ni–Ga ferromagnetic shape memory alloys, J. Mater. Sci. 46 (2011) 6224–6234.
[23] M. Vollmer, P. Krooß, C. Segel, A. Weidner, A. Paulsen, J. Frenzel, M. Schaper, G. Eggeler, H.J. Maier, T. Niendorf, Damage evolution in pseudoelastic polycrystalline Co–Ni–Ga high-temperature shape memory alloys, J. Alloys Compd. 633 (2015) 288–295.
[24] E. Karsten, G. Gerstein, O. Golovko, A. Dalinger, C. Lauhoff, P. Krooss, T. Niendorf, A. Samsonenko, H.J. Maier, Tailoring the microstructure in polycrystalline Co–Ni–Ga high-temperature shape memory alloys by hot extrusion, Shape Memory and Superelasticity 5 (2019) 84–94.
[25] T. Niendorf, C. Lauhoff, E. Karsten, G. Gerstein, A. Liehr, P. Krooß, H.J. Maier, Direct microstructure design by hot extrusion–high-temperature shape memory alloys with bamboo-like microstructure, Scr. Mater. 162 (2019) 127–131.
[26] M. Raventós, M. Tovar, M. Medarde, T. Shang, M. Strobl, S. Samothrakitis, E. Pomjakushina, C. Grünzweig, S. Schmidt, Laue three dimensional neutron diffraction, Sci. Rep. 9 (2019) 1–13.
[27] S. Samothrakitis, M. Raventós, J. Čapek, C.B. Larsen, C. Grünzweig, M. Tovar, M. Garcia-Gonzalez, J. Kopeček, S. Schmidt, M. Strobl, Grain morphology reconstruction of crystalline materials from Laue three-dimensional neutron diffraction tomography, Sci. Rep. 10 (2020) 1–7.
[28] G.N. Iles, S. Schorr, The HZB neutron Laue diffractometer: from E11 to FALCON, Neutron News 25 (2014) 27–29.
[29] F.J. Humphreys, M. Hatherly, Recrystallization and Related Annealing Phenomena, Elsevier, 2012.
[30] C. Braun, J.M. Dake, C.E. Krill, R. Birringer, Abnormal grain growth mediated by fractal boundary migration at the nanoscale, Sci. Rep. 8 (2018) 1–6.
[31] T. Omori, H. Iwaizako, R. Kainuma, Abnormal grain growth induced by cyclic heat treatment in Fe-Mn-Al-Ni superelastic alloy, Mater. Des. 101 (2016) 263–269.

[32] H.E. Karaca, I. Karaman, B. Basaran, Y.I. Chumlyakov, H.J. Maier, Magnetic field and stress induced martensite reorientation in NiMnGa ferromagnetic shape memory alloy single crystals, Acta Mater. 54 (2006) 233–245.
[33] J.I. Pérez-Landazábal, V. Recarte, C. Gómez-Polo, C. Seguí, E. Cesari, J. Dutkiewicz, Magnetic behavior in Ni–Fe–Ga martensitic phase, Mater. Sci. Eng. A 481 (2008) 318–321.
[34] M. Sofronie, F. Tolea, V. Kuncser, M. Valeanu, Martensitic transformation and accompanying magnetic changes in Ni–Fe–Ga–Co alloys, J. Appl. Phys. 107 (2010) 113905.
[35] C. Wang, A.A. Levin, L. Nasi, S. Fabbrici, J. Qian, C.E.V. Barbosa, S. Ouardi, J. Karel, F. Albertini, H. Borrmann, et al., Chemical synthesis and characterization of γ-Co_2NiGa nanoparticles with a very high curie temperature, Chem. Mater. 27 (2015) 6994–7002.
[36] C. Wang, A.A. Levin, S. Fabbrici, L. Nasi, J. Karel, J. Qian, C.E.V. Barbosa, S. Ouardi, F. Albertini, W. Schnelle, et al., Tunable structural and magnetic properties of chemically synthesized dual-phase Co_2NiGa nanoparticles, J. Mater. Chem. C 4 (2016) 7241–7252.
[37] C. Wang, A.A. Levin, J. Karel, S. Fabbrici, J. Qian, C.E. ViolBarbosa, S. Ouardi, F. Albertini, W. Schnelle, J. Rohlicek, et al., Size-dependent structural and magnetic properties of chemically synthesized Co-Ni-Ga nanoparticles, Nano Res. 10 (2017) 3421–3433.
[38] O. Heczko, S. Fähler, T.M. Vasilchikova, T.N. Voloshok, K.V. Klimov, Y.I. Chumlyakov, A.N. Vasiliev, Thermodynamic, kinetic, and magnetic properties of a $Ni_{54}Fe_{19}Ga_{27}$ magnetic shape-memory single crystal, Phys. Rev. B 77 (2008) 174402.
[39] A. Planes, L. Mañosa, M. Acet, Magnetocaloric effect and its relation to shape-memory properties in ferromagnetic Heusler alloys, J. Phys. Condens. Matter 21 (2009) 233201.
[40] E. Dogan, I. Karaman, N. Singh, A. Chivukula, H.S. Thawabi, R. Arroyave, The effect of electronic and magnetic valences on the martensitic transformation of CoNiGa shape memory alloys, Acta Mater. 60 (2012) 3545–3558.
[41] V.A. Chernenko, E. Cesari, V.V. Kokorin, I.N. Vitenko, The development of new ferromagnetic shape memory alloys in Ni-Mn-Ga system, Scr. Metall. Mater. 33 (1995) 1239–1244.
[42] C. Craciunescu, Y. Kishi, T.A. Lograsso, M. Wuttig, Martensitic transformation in Co_2NiGa ferromagnetic shape memory alloys, Scr. Mater. 47 (2002) 285–288.
[43] A. Williams, V. Moruzzi, A. Malozemoff, K. Terakura, Generalized Slater-Pauling Curve for Transition-Metal Magnets, IEEE Transactions on Magnetics 19, 1983.
[44] N. Singh, E. Dogan, I. Karaman, R. Arróyave, Effect of configurational order on the magnetic characteristics of co-ni-ga ferromagnetic shape memory alloys, Phys. Rev. B 84 (2011) 184201.
[45] K. Prusik, H. Morawiec, B. Kostrubiec, M. Prewendowski, G. Dercz, K. Ziewiec, The effect of γ-phase particles on microstructure and properties of Co-Ni-Ga alloys, Eur. Phys. J. Spec. Top. 158 (2008) 155–159.
[46] Y. Li, Y. Xin, L. Chai, Y. Ma, H. Xu, Microstructures and shape memory characteristics of dual-phase Co–Ni–Ga high-temperature shape memory alloys, Acta Mater. 58 (2010) 3655–3663.